Journal of Materials Chemistry C

ROYAL SOCIETY OF CHEMISTRY

PAPER

View Article Online
View Journal | View Issue



Cite this: J. Mater. Chem. C, 2022, 10, 11286

# Isomerization of two-dimensional non-fullerene electron acceptor materials for developing high-performance organic solar cells†

Yezi Yang,[a] Chuang Yao,*[a] Lei Li,[a] Maolin Bo,[a] Meng He*[b] and Jinshan Wang*[b]

Although the power conversion efficiency of organic solar cells has recently exceeded 19% benefiting from the development of non-fullerene acceptors (NFAs), the electron affinity and electron mobility of NFAs still lag behind those of fullerene acceptors. Therefore, it is necessary to investigate a design rule that can break the currently used A–D–A linear strategy. In our early study, we have proposed a kind of two-dimensional (2D) NFA containing four electron-withdrawing end groups, which exhibited better electron affinity and electron mobility than those of typical linear NFAs. As we know, isomerism is one of the major factors affecting the properties of materials. Herein, three isomeric 2D NFAs based on a 2D fused-ring core (naphthalene) and four electron-withdrawing end groups, **2D-ICH**, **d-2D-ICH** and **b-2D-ICH**, are reported, which exhibited a similar chemical structure but different symmetries. The molecular structures, intramolecular interactions, energy level, electron affinity, electrostatic potential, absorption spectra, exciton binding energy, electron mobility, solubility and chemical stability of these isomers were investigated. The results indicated that the isomerism of the conjugated backbone is an efficient method to turn the optoelectronic properties of NFA materials. **d-2D-ICH** shows an appropriate LUMO energy of −3.99 eV, a high electron affinity of 3.34 eV, higher integrated absorption intensity and smaller exciton binding energy than those of **Y6**, good solubility of 52 mg $mL^{-1}$ in chlorobenzene, the highest chemical stability, and high electron mobility of $9.42 \times 10^{-4}$ $cm^2$ $V^{-1}$ $s^{-1}$. This demonstrated that numerous critical factors including absorption intensity, exciton separation, chemical stability, and charge mobility of **d-2D-ICH** are superior to those of widely used **Y6**. We propose that **d-2D-ICH** will be an excellent candidate for the development of next-generation NFAs for high-performance organic solar cells.

Received 7th June 2022,
Accepted 11th July 2022

DOI: 10.1039/d2tc02373c

rsc.li/materials-c



## Introduction

In last decades, organic solar cells (OSCs) have gone through rapid development due to their advantages of lightweight, semi-transparency, solution-processability and low cost.[1,2] Conventional OSCs consist of mixed electron donor materials and electron acceptor materials to form a bulk heterojunction, which can generate donor and acceptor interfaces to accelerate exciton dissociation. Various donor and acceptor materials have been developed to improve the performance of OSCs.[3–7] Especially for the appearance of non-fullerene acceptors (NFAs) in recent years, the power conversion efficiency of single-junction OSCs has made a great improvement[8–11] and the highest one has exceeded 19%.[12] These achievements mainly benefit from the distinguished advantages of NFAs such as strong absorption of visible and near-infrared solar energy, tuning of absorption and electronic energy levels, and easy and flexible synthetic method. Although NFAs have so many advantages, they exhibit smaller electron affinity and lower electron mobility than those of fullerene-based electron acceptors.[13–15] Therefore, to further improve the performance of OSCs, increasing the electron affinity and electron mobility of NFAs will be an important path.

Currently, widely used NFAs consist of two strongly electron-withdrawing end groups connected by a planar fused-ring core to form an A–D–A-type linear structure.[2,16] Although various efforts have been made to investigate the effect of electron-withdrawing

[a] Chongqing Key Laboratory of Extraordinary Bond Engineering and Advance Materials Technology (EBEAM), School of Materials Science and Engineering, Yangtze Normal University, Chongqing 408100, P. R. China. E-mail: yaochuang@yznu.cn

[b] School of Materials Science and Engineering, Yancheng Institute of Technology, Yancheng 224051, P. R. China. E-mail: hemeng315@163.com, wangjinshan@ycit.cn

† Electronic supplementary information (ESI) available. See DOI: https://doi.org/10.1039/d2tc02373c

end groups,[11,17] fused-ring core,[18] and side chains,[4,19] the linear structure is still the most commonly used. In our previous study, we have proposed a quad-rotor-shaped two-dimensional (2D) NFA, BFT-TN, which exhibits larger electron affinity (3.45 eV) than that of ITIC (2.90 eV) and much higher electron mobility ($5.32 \times 10^{-3}$ $cm^2$ $V^{-1}$ $s^{-1}$) than that of ITIC ($8.20 \times 10^{-4}$ $cm^2$ $V^{-1}$ $s^{-1}$).[20] We also demonstrated that as the degree of conjugation of these 2D NFAs increased, the spectrum red-shifted, the integrated absorption intensity enhanced, and the hole–electron coulombic attraction decreased.[21] Therefore, further investigation of this kind of 2D NFA should be made.

Isomerism is the phenomenon in which more than one compounds have the same chemical formula but different chemical structures and properties, which is very important in chemistry. Isomers can be divided into two broad classes. Substances that differ in their connectivity are constitutional isomers. Isomers that have the same connectivity but different arrangements of the atoms in space are stereoisomers.[22] The constitutional isomerization strategy has been used in many works to develop high-performance acceptor materials. Yang and co-workers investigated the performance of constitutional isomers of ITIC with *para*-alkyl-phenyl substitution and demonstrated that the side chain isomerization is an easy and convenient way to further improve the performance of OSCs.[7] Recently, Lai and co-workers studied two isomeric acceptors based on acetoxy and methyl ester end group substituents.[23] The results indicated that isomerism can fine tune the energy levels, adjust the absorption spectra and regulate the energy loss. Therefore, constitutional isomerization strategy is an effective way to fine tune the optoelectronic properties of materials. Although, as discussed above, 2D NFA materials are a new type of electron acceptors for developing high-performance NFA materials, the isomerization of these materials has not been paid enough attention.

In this work, three isomeric 2D NFA materials constructed by one 2D core (naphthalene) and four 1,1-dicya-nomethylene-3-indanone end groups, **2D-ICH**, **d-2D-ICH**, and **b-2D-ICH**, (Fig. 1) were investigated. The effects of isomerization on their optoelectronic properties (containing energy levels, electron affinity, absorption spectra, exciton binding energy and electron mobility) and solubility in chloroform were studied by theoretical calculations and machine learning. The isomer **d-2D-ICH** exhibited larger electron affinity, stronger absorption intensity, smaller exciton binding energy, higher chemical stability and higher electron mobility than those of **Y6**. At the same time, linked with 4-ethyloctane as the side chain, it shows good solubility in chlorobenzene, which will facilitate the preparation of OSCs by a solution-processed method. These results imply that the isomerism of conjugated backbone is an efficient method to tune the optoelectronic properties of NFA materials. Simultaneously, these results indicate that **d-2D-ICH** is suitable as an important candidate for the development of next-generation NFAs for high-performance OSCs.

## Computational method

### Quantum chemical calculations

The ground-state geometry optimization of **2D-ICH**, **d-2D-ICH** and **b-2D-ICH** was calculated at the B3LYP/def2-SVP level with the atom-pairwise dispersion correction[23] to the DFT energy with Becke–Johnson (D3BJ).[24] The highest occupied molecular orbital (HOMO) and lowest unoccupied molecular orbital (LUMO) energy levels, adiabatic electron affinities (AEA) and

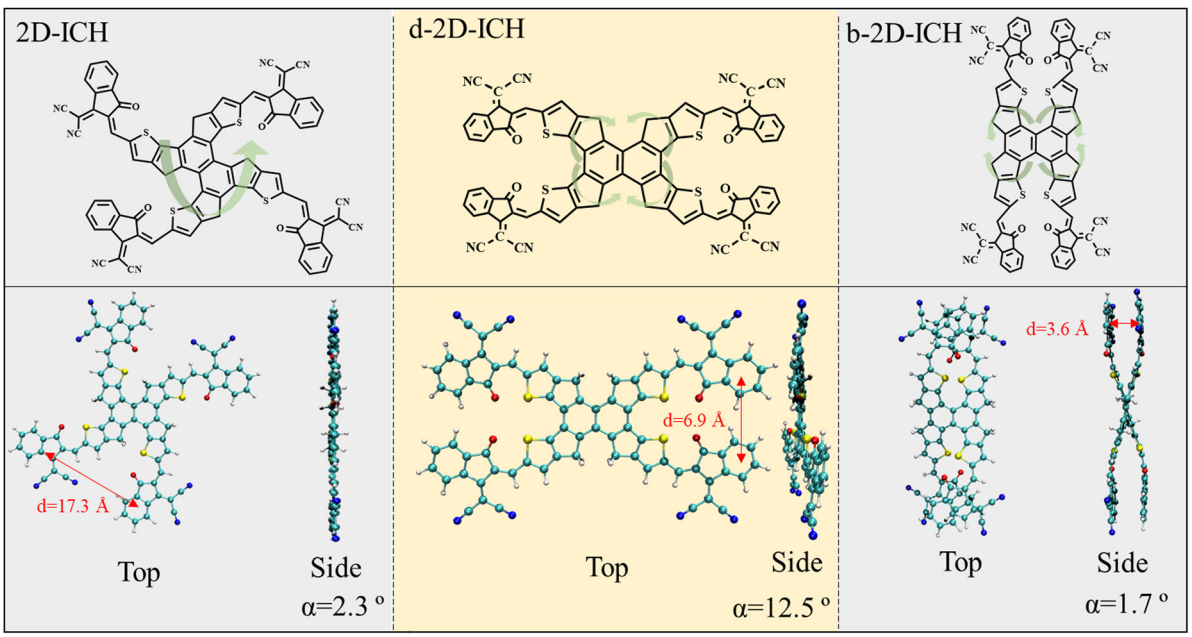


Fig. 1 Chemical structures and top/side view for the optimized structures of **2D-ICH**, **d-2D-ICH**, and **b-2D-ICH**. Dihedral angle ($\alpha$) and center distance ($d$) of the nearest adjacent end groups are listed at the bottom.

adiabatic ionization energy (AIP), electron reorganization energies ($\lambda^-$) and spatial distribution of the frontier molecular orbitals were calculated at the B3LYP/def2-TZVP level. PBE0/def2-SVPD was used to investigate the absorption spectra of these materials. The atom-pairwise dispersion correction (D3ZERO) was used to account for the major parts of dispersion force contribution to the energy.[25] The noncovalent interaction (NCI) method known as reduced density gradient (RDG) method,[26] electrostatic potential (ESP), and excited state analysis were obtained using the Multiwfn 3.8 package.[27] All quantum chemical calculations were carried out based on the ORCA Revision 5.0.1 program.[28]

### Machine learning

The solubility of **Y6**, **2D-ICH**, **d-2D-ICH**, and **b-2D-ICH** in 42 common solvents at 298 K was predicted by a machine learning model built in our previous work.[29] In this model, four 4-ethyloctane molecules were linked to each molecule of **2D-ICH**, **d-2D-ICH**, and **b-2D-ICH** as side chains. This model is based on Random Forest regression algorithm with a small set of descriptors (7 bits), which consist of area (molecular surface area), $\sigma^2_+$ (positive ESP variance when analyzing the distribution of ESP on vdW surface) and $\sigma^2_-$ (negative ESP variance when analyzing the distribution of ESP on the vdW surface) of solvent and solute calculated by quantum chemistry and temperature. The geometries of these molecules with side chains were first optimized using the DS-PAW software[30] integrated in the Device Studio Program.[31] Further geometry optimization and single-point energy calculation were carried out at the B3LYP/def2-SVP and B3LYP/def2-TZVPD level respectively by ORCA 5.0.1. Then the surface descriptors of these materials were calculated by Multiwfn based on the wavefunction generated by the single-point energy calculations.

### Multiscale simulations

The electron mobilities of **Y6**, **2D-ICH**, **d-2D-ICH**, and **b-2D-ICH** amorphous thin films were evaluated by a multiscale simulation based on quantum chemical calculations, molecular dynamics (MD) simulations and Monte Carlo (MC) calculations.

**MD simulations.** As the side chains can efficiently affect the packing of molecules during the MD simulations, four 4-ethyloctane side chains were introduced when processing the MD simulations of **2D-ICH**, **d-2D-ICH**, and **b-2D-ICH** amorphous thin films. MD simulations were carried out using the GROMACS program with general amber force field (GAFF).[32] The restrained electrostatic potential (RESP) atomic charge calculated by Multiwfn, was used for the GAFF. The MD simulation processes were built and imitated using the following procedures: (1) 520 and 420 molecules of **Y6** and these 2D NFAs (**2D-ICH**, **d-2D-ICH** or **b-2D-ICH**) were randomly inserted in a large box ($20 \times 20 \times 20$ nm$^3$) to generate the initial geometry; (2) 50 000 steps of the steepest descent were conducted on the system to remove the undesired forces and structural distortion; (3) *NVT* models were carried out at 300 K for 100 ps to naturally close the gap between molecules; (4) *NPT* ensemble were used to compress the box size at 300 K for 50 ps; (5) models in the *NPT* ensemble were annealed between 420 and 300 K for six times in 2.0 ns; and (6) the system was kept at a temperature of 300 K for 10 ns to achieve a completely converged system.

**MC simulations.** As the internal reorganization energies are large and the electronic couplings are not strong for these systems, we employed the hopping model to calculate the electron mobility of **Y6**, **2D-ICH**, **d-2D-ICH**, and **b-2D-ICH**. The hopping rate from one molecule to the adjacent molecules can be described by the Marcus formula,[33] as follows:

$$k_{ij} = \frac{1}{\hbar^2}|V_{ij}|^2\sqrt{\frac{\pi}{\lambda k_B T}}\exp\left(-\frac{(\lambda + \Delta G_{ij})}{4k_B T}\right) \quad (1)$$

where $\hbar$ is reduced Planck's constant, and $V_{ij}$ is the transfer integral between the $i$th and $j$th molecules calculated using Zerner's intermediate neglect of a differential overlap (ZINDO) method.,[34] $k_B$ is the Boltzmann constant, $T$ is the temperature and is set as 300 K in this work, $\lambda$ denotes the reorganization energy and $\Delta G_{ij}$ is the free energy estimated to be the LUMO energy difference of $i$th and $j$th molecules.

The MC calculations were carried out as described in our previous work.[35–37] The adjacent molecular pairs (the shortest interatomic distance is less than 0.5 nm) for each molecule under periodic conditions based on the model of amorphous films were obtained from the MD simulations. The center-of-mass (COM) of each molecular backbone was utilized as the hopping point in the MC simulations. During the hopping process, we first randomly selected one molecule ($i$) as the initial charge center. Then, the charge hops between the center molecule $i$ and its adjacent molecule ($j$) with a probability of $P_{ij} = k_{ij}/\Sigma k_{ij}$. The hopping time was defined as $1/k_{ij}$, and the hopping distance was taken to be the molecular COM($i$)-COM($j$) distance. Finally, we used the hopping coordinate and time to build the relationship between square diffusion displacement and the diffusion time to estimate the charge diffusion coefficient.

## Results and discussion

Isomerism is one of the major factors affecting the properties of materials. Here, we first investigated three isomeric 2D NFA materials by isomerization of the conjugated backbone. The optoelectronic properties (containing energy levels, electron affinity, absorption spectra, exciton binding energy and electron mobility) and solubility in chloroform were studied by theoretical calculations and machine learning.

### Geometry and intramolecular interactions

Three isomers constructed by one 2D core (naphthalene) and four 1,1-dicya-nomethylene-3-indanone end groups, namely, **2D-ICH**, **d-2D-ICH**, and **b-2D-ICH** were designed, as shown in Fig. 1. These isomers are isomerized by changing the connection between naphthalene and fluorene. This is a new isomerization strategy by isomerizing the conjugated backbone, which is different from the commonly used side chain isomerization.

 

The top and side views for the optimized structures of these isomers are depicted at the bottom of Fig. 1. The center distance and dihedral angle of the nearest adjacent end groups of **2D-ICH** are 17.3 Å and 2.3°, respectively, indicating that it presents an expended coplanar geometry. In **d-2D-ICH**, due to the existence of steric effect, the coplanar geometry is destroyed and the dihedral angle of the adjacent end groups is 12.5°. The center distance of the nearest adjacent end groups decreased to 6.9 Å. Compared with **2D-ICH** and **d-2D-ICH**, **b-2D-ICH** shows a completely different geometry and exhibits an overlapping structure of the nearest adjacent end groups. These overlapped end groups are approximately parallel with a dihedral angle of 1.7°. At the same time, their center distance is only 3.6 Å, which is within the range of a typical π–π interaction distance (3.3–3.8 Å).[38] These results indicate the existence of strong intramolecular interactions between the end groups in **b-2D-ICH**.

To better investigate the intramolecular interactions, the noncovalent interaction (NCI) method known as reduced density gradient (RDG) method[26] was used to study the weak interaction in these isomers. The color filling maps to the RDG isosurfaces of these isomers obtained from Multiwfn[27] are shown in Fig. 2. From the color-filled RDG isosurface, we identified different types of noncovalent interaction in them, as shown in Fig. 2. As shown by the scar bar, the bluer implies stronger attractive interaction, the redder indicates stronger repulsion interaction and the region marked by green can be identified as vdW interaction region. In **2D-ICH**, there are three kinds of noncovalent intramolecular interactions (H···π, S···O and H···S), which have been demonstrated by the topological analysis of a similar structure in our previous work.[20] In addition to H···π and S···O intramolecular interactions, **d-2D-ICH** has obvious vdW interaction and steric effect, which distorted the molecular structure, as shown in Fig. 1. There is a green isosurface between the end groups of **b-2D-ICH**, which can be identified as π–π interaction region combined with the above-discussed result. It is due to the existence of π–π interaction that the molecule of **b-2D-ICH** shows a completely overlapping structure between the adjacent end groups. Obviously, there are red RDG isosurfaces at the center of all rings in these isomers, which indicate strong steric effects in the ring.

### Electronic properties

As HOMO and LUMO energy levels dominate the exciton separation, charge transportation and open circuit voltage of OSCs, the HOMO and LUMO energy levels of **2D-ICH**, **d-2D-ICH** and **b-2D-ICH** compared with the widely used electron acceptor **Y6** are shown in Fig. 3(a). **2D-ICH**, **d-2D-ICH** and **b-2D-ICH** exhibit lower-lying LUMOs than that of **Y6**, which will result in

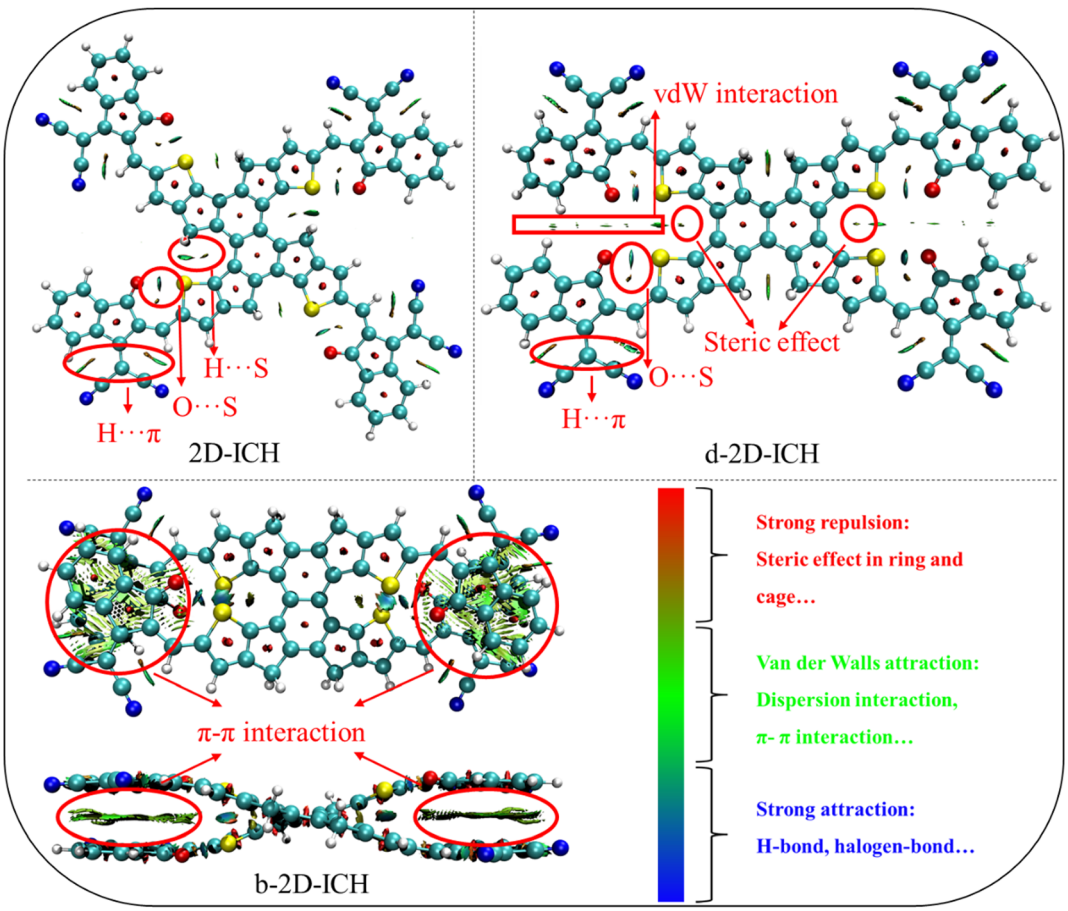


Fig. 2 Color filling maps to the reduced density gradient isosurfaces of **2D-ICH**, **d-2D-ICH**, and **b-2D-ICH**.

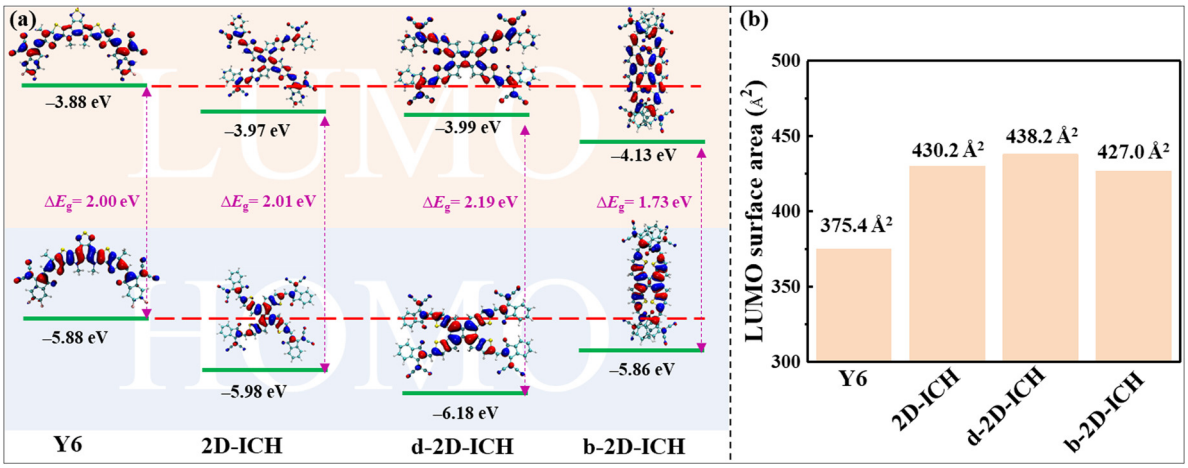


Fig. 3 HOMO and LUMO energy levels and spatial distribution (a), and surface area (b) of LUMO with an isosurface of 0.02 a.u. for **Y6**, **2D-ICH**, **d-2D-ICH**, and **b-2D-ICH**.



Table 1 HOMO and LUMO energy levels, HOMO and LUMO band gap ($\Delta E_g$), adiabatic electron affinities (AEA), adiabatic ionization energy (AIP), and electron reorganization energies ($\lambda^-$) of **Y6**, **2D-ICH**, **d-2D-ICH**, and **b-2D-ICH**

| | HOMO (eV) | LUMO (eV) | $\Delta E_g$ (eV) | AEA (eV) | AIP (eV) | $\lambda^-$ (eV) |
|---|---|---|---|---|---|---|
| **Y6** | −5.88 | −3.88 | 2.00 | 3.12 | 6.60 | 0.14 |
| **2D-ICH** | −5.98 | −3.97 | 2.01 | 3.33 | 6.67 | 0.15 |
| **d-2D-ICH** | −6.18 | −3.99 | 2.19 | 3.34 | 6.84 | 0.13 |
| **b-2D-ICH** | −5.86 | −4.13 | 1.73 | 3.45 | 6.54 | 0.20 |

a larger current density when combined with a large-bandgap donor material.[39] The LUMO energy levels **2D-ICH**, **d-2D-ICH** and **b-2D-ICH** are 0.09, 0.11 and 0.25 eV, respectively, lower than that of **Y6**, which implied that **2D-ICH**, **d-2D-ICH** and **b-2D-ICH** will have stronger electronic attraction than that of **Y6**. It is confirmed by the calculated adiabatic electron affinities (AEA) of **Y6** (3.12 eV), **2D-ICH** (3.33 eV), **d-2D-ICH** (3.34) and **b-2D-ICH** (3.45 eV), as presented in Table 1. Although **b-2D-ICH** exhibits stronger electronic attraction, the LUMO energy level is much lower, which will dramatically reduce the open circulate voltage of OSCs. Therefore, when focusing on the energy levels, **2D-ICH** and **d-2D-ICH** will have more advantages. The HOMO and LUMO energy band gaps of **Y6**, **2D-ICH**, **d-2D-ICH**, and **b-2D-ICH** are 2.00, 2.00, 2.20 and 1.73 eV, respectively. This result indicates that compared with **Y6**, 2D-ICH will exhibit similar absorption peaks, and **d-2D-ICH** and **b-2D-ICH** will show blue- and red-shifted absorption peaks, respectively. It is obvious that the spatial distribution of LUMO delocalized on the whole conjugation backbone of **Y6** and these 2D isomers (Fig. 3(a)). To quantitatively describe the distribution of LUMOs, the surface area of LUMO with an isosurface of 0.02 for **Y6** and these isomers was calculated using Multiwfn, as shown in Fig. 3(b). The LUMO surface area of **2D-ICH** (430.2 Å$^2$), **d-2D-ICH** (438.2 Å$^2$) and **b-2D-ICH** (427.0 Å$^2$) is larger than that of **Y6** (375.4 Å$^2$), which indicates that when an electron is obtained in these 2D isomers, the delocalization region of this electron will be larger than **Y6**.

The electron reorganization energies ($\lambda^-$) of **Y6**, **2D-ICH**, **d-2D-ICH** and **b-2D-ICH** are 0.14, 0.15, 0.13 and 0.20 eV, respectively. This is a key parameter affecting the electron mobility of materials, which is inversely proportional to the hopping rate, as shown in eqn (1).

To investigate the ESP distribution of these 2D isomers, the ESP distribution of **Y6**, **2D-ICH**, **d-2D-ICH** and **b-2D-ICH** is depicted in Fig. 4(a). Obviously, in all these molecules, the ESP values on the conjugated backbone are almost positive. The maximum ESP values of **Y6**, **2D-ICH**, **d-2D-ICH** and **b-2D-ICH** are 41.5, 25.6, 36.7 and 32.8 kcal mol$^{-1}$, respectively. The results indicate that these 2D isomers show similar electron-accepting ability to that of **Y6**. The negative ESP values are mainly distributed around −C≡N and ketone groups. The minimum values are −33.0, −29.2, −29.0 and −28.0 kcal mol$^{-1}$, respectively, distributed around −C≡N groups of **Y6** and these 2D isomers. This is mainly caused by the strong electron-withdrawing property of −C≡N groups. To quantitatively study the distribution of ESP, we mapped the ESP area distribution, as shown in Fig. 4(b). The area percentages of **2D-ICH**, **d-2D-ICH** and **b-2D-ICH** with ESP values larger than 0 are 75%, 74% and 73%, respectively, which are larger than that of **Y6** (72%). Combined with the results of AEA as shown in Table 1, we suggest that these 2D isomers will have sufficient electron-affinity, even larger than that of **Y6**.

### Electronic absorption spectra analysis

Strong absorption in visible and NIR spectrum regions is an essential characteristic of excellent FREAs, which will generate more excitons under the sunlight to increase the power conversion efficiency. Here, we investigated the electronic absorption spectra of **Y6**, **2D-ICH**, **d-2D-ICH** and **b-2D-ICH** in chloroform by time-dependent density functional theory (TDDFT). The spectrum broadened by Multiwfn with the molar absorption coefficient as the ordinate is shown in Fig. S1(a) (ESI†). Compared with **Y6**, the absorption spectrum of **2D-ICH** shows a similar absorption peak around 700 nm and strong absorption peaks in the

 

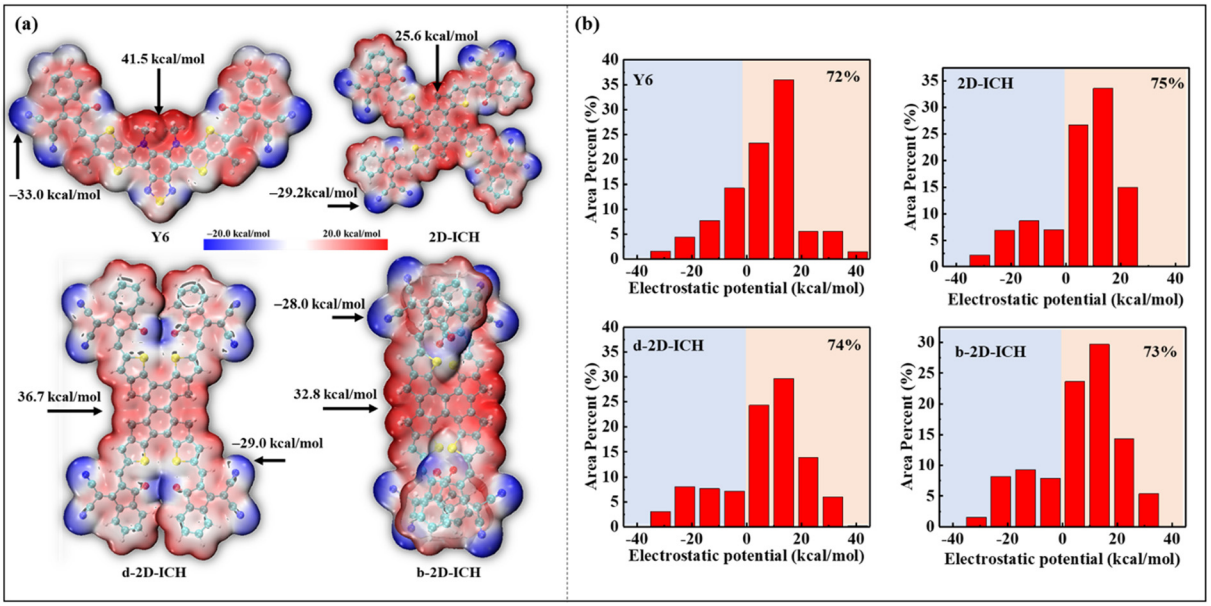


Fig. 4 ESP distribution (a) and area percentage (b) of **Y6**, **2D-ICH**, **d-2D-ICH**, and **b-2D-ICH**. Maximum and minimum values of the ESP distribution are added in (a) and percentage with an ESP value larger than 0 of these molecules is added in (b).

blue-shifted region at 626 and 538 nm. **d-2D-ICH** exhibits blue-shifted and broadened absorption bands around 500–600 nm. Two significant absorption peaks appeared in the absorption spectrum of **b-2D-ICH**, which are located in the red and green regions, respectively. To quantitatively investigate the absorption intensity, we calculated the integrated intensity of these spectra, as shown in Fig. S1(b), (ESI†) which are $3.40 \times 10^7$, $4.12 \times 10^7$, $4.36 \times 10^7$ and $4.14 \times 10^7$ for **Y6**, **2D-ICH**, **d-2D-ICH** and **b-2D-ICH**, respectively. This result indicates that these 2D isomers will have stronger absorption of sunlight than that of **Y6**, which will contribute to improve the performance of the corresponding OSCs. It is obvious that **d-2D-ICH** has the strongest absorption intensity in these 2D isomers, which indicates that it has significant advantages in absorbing sunlight.

To further identify the contribution of each excited state to the absorption spectra, the detailed electron excited states calculated by TDDFT of **Y6**, **2D-ICH**, **d-2D-ICH** and **b-2D-ICH** were analyzed, as shown in Fig. 5. The absorption spectrum of **Y6** is mainly dominated by the $S_0 \rightarrow S_1$ transition with a high oscillator strength ($f$) of 2.08 and an absorption wavelength ($\lambda$) at 700 nm. Analyzing the electron and hole distribution of this excitation, we noticed that during the excitation, the electron transformed from the center to the end groups. As shown in Fig. 5(b), the absorption spectrum of **2D-ICH** consists of three main excitations with $f$ larger than 0.5, which are $S_0 \rightarrow S_1$ ($\lambda$: 702 nm, $f$: 1.04), $S_0 \rightarrow S_3$ ($\lambda$: 626 nm, $f$: 0.95) and $S_0 \rightarrow S_5$ ($\lambda$: 538 nm, $f$: 1.72). The absorption spectra of **d-2D-ICH** is dominated by the excitations of $S_0 \rightarrow S_1$ ($\lambda$: 663 nm, $f$: 1.31), $S_0 \rightarrow S_2$ ($\lambda$: 623 nm, $f$: 0.78) and $S_0 \rightarrow S_4$ ($\lambda$: 557 nm, $f$: 2.21), as shown in Fig. 5(c). The electron and hole distributions of the excitations of **2D-ICH** and **d-2D-ICH** were depicted in a related place, which demonstrated that during these excitations, the electrons and holes are delocalized around the center region and exhibit a degree of overlap. **b-2D-ICH** also exhibits three main excitations (Fig. 5(d)) with $f$ larger than 0.5, which are $S_0 \rightarrow S_1$ ($\lambda$: 758 nm, $f$: 1.54), $S_0 \rightarrow S_6$ ($\lambda$: 561 nm, $f$: 1.55) and $S_0 \rightarrow S_7$ ($\lambda$: 558 nm, $f$: 0.72). Herein, the electron and hole distribution of $S_0 \rightarrow S_1$ exhibits a similar overlap, as shown in 2D-ICH and **d-2D-ICH**, while those of $S_0 \rightarrow S_6$ and $S_0 \rightarrow S_7$ exhibit obvious separation of the electron and hole. To compare the overlapping extent of holes and electrons quantitatively, we characterized the $S_r$ index[20] of each excited state, as summarized in Table 2. The $S_r$ index of **b-2D-ICH** is between 0.006 and 0.023, which is much smaller than that of **2D-ICH** (0.561–0.694), **d-2D-ICH** (0.610–0.710) and **Y6** (0.650). This result also indicates less overlap between the hole and the electron of excitons in **b-2D-ICH**, which can result in a smaller exciton binding energy. Simultaneously, we studied the molecular orbital (MO) contribution for each transition process by Multiwfn, as summarised in Table 2. The absorption spectrum of **Y6** is dominated by the transition between HOMO and LUMO, whereas HOMO−1, HOMO, LUMO, LUMO+1, and LUMO+4 contribute to the transition of **2D-ICH**, **d-2D-ICH** and **b-2D-ICH**, which may be due to the increased symmetry of these 2D isomers.

The difficulty of exciton separation will also affect the efficiency of OSCs. Here, we investigated the coulombic attraction ($E_c$) and exciton binding energy ($E_b$) of each electronic excited state. The definitions of $E_c$ and $E_b$ are shown as in eqn (2)[20] and eqn (3):[40]

$$E_c = \iint \frac{\rho^{hole}(r_1)\rho^{electron}(r_2)}{|r_1 - r_2|} dr_1 dr_2 \quad (2)$$

$$E_b = \text{AIP-AEA-}E_{s1} \quad (3)$$

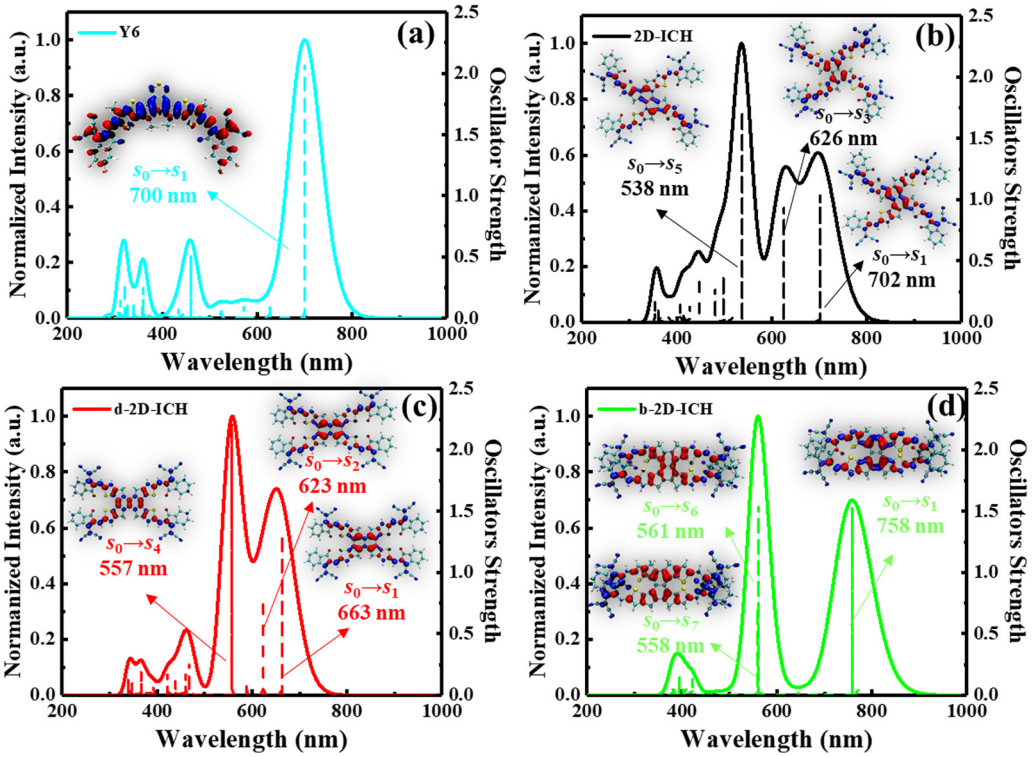


Fig. 5 TDDFT-calculated detailed electron excited states contribute to the absorption spectra of **Y6** (a), **2D-ICH** (b), **d-2D-ICH** (c) and **b-2D-ICH** (d), and the electron (blue) and hole (red) distribution of the excitations with an oscillator strength larger than 0.5 is inserted.

Table 2 Excited state analysis ($\lambda$, $f$, MO contribution, $D_{index}$, $S_r$ index, $E_c$, and $E_b$) of **Y6**, **2D-ICH**, **d-2D-ICH**, and **b-2D-ICH** with an oscillator strength larger than 0.5

| | Excited states | $\lambda$ (nm) | $f$ | MO contribution[a] | $S_r$ index (a.u.) | $E_c$ (eV) | $E_b$[b] (eV) |
|---|---|---|---|---|---|---|---|
| **Y6** | $S_0 \rightarrow S_1$ | 700 | 2.08 | H → L (97%) | 0.65 | 2.55 | 1.72 |
| **2D-ICH** | $S_0 \rightarrow S_1$ | 702 | 1.04 | H → L (98%) | 0.69 | 2.18 | 1.51 |
| | $S_0 \rightarrow S_3$ | 626 | 0.95 | H → L+2 (95%) | 0.56 | 2.08 | |
| | $S_0 \rightarrow S_5$ | 538 | 1.72 | H−1 → L (93%) | 0.65 | 1.98 | |
| **d-2D-ICH** | $S_0 \rightarrow S_1$ | 663 | 1.31 | H → L (95%) | 0.63 | 2.12 | 1.63 |
| | $S_0 \rightarrow S_2$ | 623 | 0.78 | H−1 → L (95%) | 0.71 | 2.07 | |
| | $S_0 \rightarrow S_4$ | 557 | 2.21 | H−1 → L+1 (93%) | 0.61 | 1.98 | |
| **b-2D-ICH** | $S_0 \rightarrow S_1$ | 758 | 1.54 | H → L (96%) | 0.02 | 0.77 | 1.45 |
| | $S_0 \rightarrow S_6$ | 561 | 1.55 | H−1 → L+1 (72%), H → L+4 (23%) | 0.01 | 0.69 | |
| | $S_0 \rightarrow S_7$ | 558 | 0.72 | H−1 → L+1 (23%), H → L +4(23%) | 0.02 | 0.62 | |

[a] H = HOMO, L = LUMO, H−1 = HOMO−1, L+1 = LUMO+1. [b] $E_b$ = AIP-AEA-$E_{s1}$.

$\rho_{hole}(r_1)$ and $\rho_{electron}(r_2)$ represent the hole and electron density at $r_1$ and $r_2$, respectively. $E_{s1}$ represents the excitation energy of $S_0 \rightarrow S_1$. The calculated $E_c$ values of each excited state are summarized in Table 2. **Y6** (1.72 eV) exhibits a higher $E_c$ than that of **2D-ICH** (1.98–2.18 eV), **d-2D-ICH** (1.98–2.12 eV) and **b-2D-ICH** (0.62–0.77 eV), which indicated that the excitons generated in these 2D isomers are easier to separate into free charges than those in **Y6**, and those in **b-2D-ICH** are the easiest one. It can be demonstrated by the estimated $E_b$, which is 1.72, 1.51, 1.63 and 1.45 eV for **Y6**, **2D-ICH**, **d-2D-ICH**, and **b-2D-ICH**, respectively. These results indicate that the 2D isomers **2D-ICH**, **d-2D-ICH** and **b-2D-ICH** can facilitate the separation of excitons to generate free charges.

### Electron mobilities

In addition to energy levels, absorption intensity and exciton separation, the hole and electron mobility of electron donor material and electron acceptor material plays a decisive role in the performance of OSCs. High electron mobility is an important property for excellent electron acceptor materials. A multi-scale simulation method described in the computational method section was used to study the electron mobility of **Y6**, **2D-ICH**, **d-2D-ICH** and **b-2D-ICH** in amorphous films. As the side chains can efficiently affect the packing of molecules during the MD simulations, four 4-ethyloctane side chains were introduced when processing the MD simulations of these 2D isomers to build up the amorphous thin films. The molecular

 

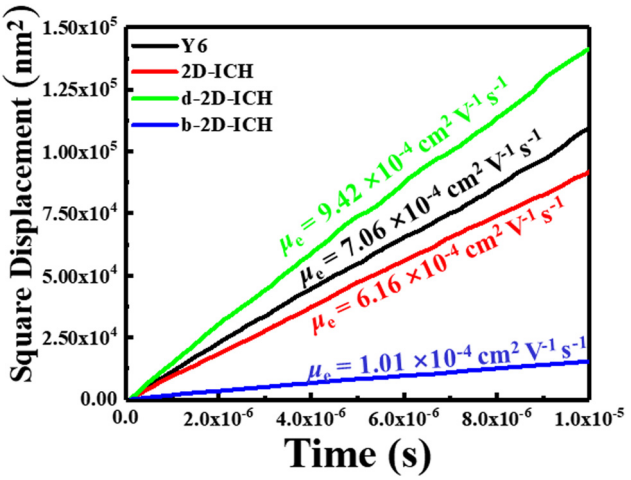


Fig. 6 Square displacement of averages over 2000 times *versus* the simulation of **Y6**, **2D-ICH**, **d-2D-ICH**, and **b-2D-ICH**.

structures are shown in Fig. S2 (ESI†). As described in Einstein's formula (eqn (4)), the electron mobility can be estimated when obtaining the electron diffusion constant:

$$\mu = \frac{eD}{k_B T}, \quad (4)$$

in which $e$ is the electron charge, $k_B$ is the Boltzmann constant, $T$ is the temperature, and $D$ is the diffusion constant. Using the multiscale simulation method, we obtained the hopping coordinate and time. Then, we built up the relationship between square diffusion displacement and the diffusion time, as shown in Fig. 6. Combined with eqn (4), the electron mobilities were estimated to be 7.06 × $10^{-4}$ $cm^2$ $V^{-1}$ $s^{-1}$, 6.16 × $10^{-4}$ $cm^2$ $V^{-1}$ $s^{-1}$, 9.42 × $10^{-4}$ $cm^2$ $V^{-1}$ $s^{-1}$ and 1.01 × $10^{-3}$ $cm^2$ $V^{-1}$ $s^{-1}$ for **Y6**, **2D-ICH**, **d-2D-ICH** and **b-2D-ICH**, respectively. The electron mobility of **Y6** estimated here is in agreement with the experiment data (3.12 × $10^{-4}$ $cm^2$ $V^{-1}$),[15] demonstrating the accuracy of this simulation method. The results indicate that the electron mobilities of **2D-ICH**, **d-2D-ICH** and **b-2D-ICH** are in the same order of magnitude as **Y6**. This result indicates that isomerism of the backbone can effectively affect the molecular structure and molecular packing in amorphous films to turn the electron mobility. We note that the mobility of **d-2D-ICH** is approximately 1.5 times that of **Y6**, which indicates that **d-2D-ICH** has significant advantages in electron transport.

## Solubility

The solubility of electron acceptor materials is a critical physical property, which can profoundly affect the morphology of the photoactive layer and the tuning of the performance of OSCs. Therefore, the solubility of electron acceptor materials should be considered during the design stage. The solubility of **Y6**, **2D-ICH**, **d-2D-ICH**, and **b-2D-ICH** in 42 common solvents at 298 K was predicted by a machine learning model built in our previous work.[29] As side chains can effectively affect the solubility of molecules, four 4-ethyloctane molecules were linked to each molecule of **2D-ICH**, **d-2D-ICH** and **b-2D-ICH**, as shown in Fig. S2 (ESI†). The molecular surface descriptors (area, $\sigma^2_+$ and $\sigma^2_-$) of these materials were calculated, as shown in Table S1 (ESI†). The solubility of **Y6** in chloroform was predicted to be 44 mg $mL^{-1}$, which is in good agreement with the experimental result (40 mg $mL^{-1}$). This result demonstrates the accuracy of this model. As shown in Fig. 7, **Y6** exhibits good solubility in some typical used solvents such as benzene (88 mg $mL^{-1}$), chlorobenzene (92 mg $mL^{-1}$), 2-butanone (78 mg $mL^{-1}$), DMF (97 mg $mL^{-1}$), DMSO (85 mg $mL^{-1}$), 1,4-dioxane (100 mg $mL^{-1}$) and pyridine (89 mg $mL^{-1}$). Although these 2D isomers have smaller solubility than that of **Y6** in almost all solvents, they also exhibit high solubility in chlorobenzene (>52 mg $mL^{-1}$), benzene (>53 mg $mL^{-1}$), DMF (>85 mg $mL^{-1}$), DMSO (>72 mg $mL^{-1}$), 1,4-dioxane (>56 mg $mL^{-1}$), chloroform (>28 mg $mL^{-1}$) and pyridine (>61 mg $mL^{-1}$), which are larger than that commonly used to prepare the photoactive

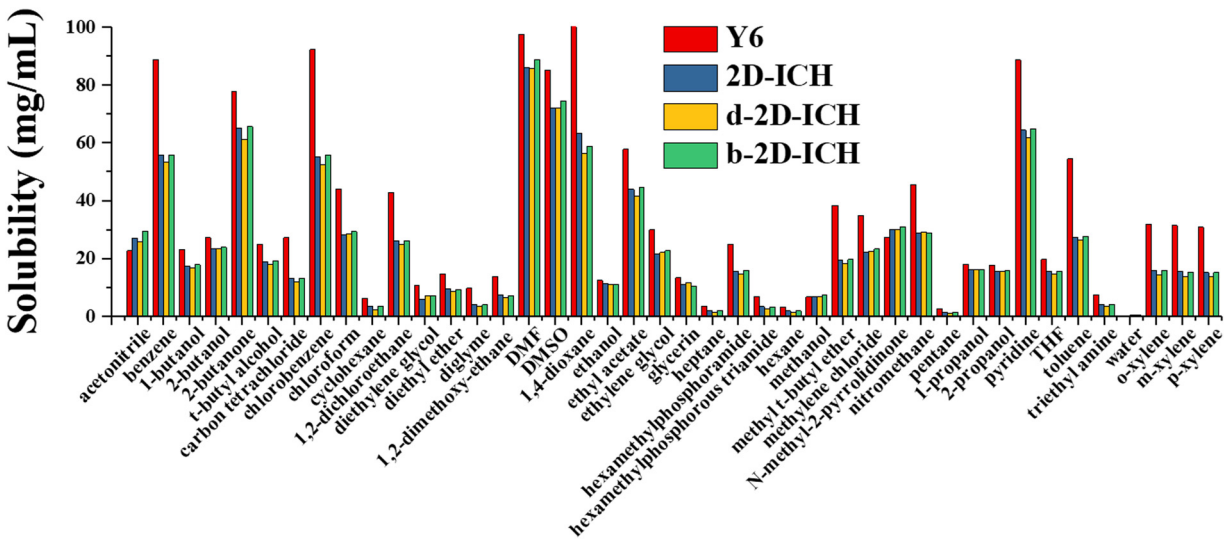


Fig. 7 Predicted solubility (mg $mL^{-1}$) of **Y6**, **2D-ICH**, **d-2D-ICH** and **b-2D-ICH** in 42 common solvents at 298 K.

Table 3 Calculated $\eta$ values in eV for investigated molecules at the B3LYP/def2-TZVP level of theory

| | Y6 | 2D-ICH | d-2D-ICH | b-2D-ICH |
|---|---|---|---|---|
| $\eta$ | 1.74 | 1.67 | 1.75 | 1.55 |

layer (total concentration of donor and acceptor $<20$ mg mL$^{-1}$).[12,41] Therefore, these 2D isomers not only have excellent optoelectronic properties, but also exhibit sufficient solubility in common solvents for preparing solution-processed OSCs.

### Chemical stability

While the function and performance of optoelectronic materials were highly important, their stability also needs to be addressed if these materials have to find their way in industrial applications. Therefore, it is necessary to characterize the stability of these 2D isomers. The absolute chemical hardness ($\eta$) based on the molecular orbital theory was utilized to evaluate the chemical stability of these 2D isomers and calculated using operational definitions as follows:[36]

$$\eta = \frac{1}{2}\left(\frac{\partial \mu}{\partial N}\right) = \frac{1}{2}\left(\frac{\partial^2 E}{\partial N^2}\right) = \frac{\mathrm{IP} - \mathrm{EA}}{2} \quad (5)$$

where $\mu$, $N$, IP and EA represent the chemical potential, total electron number, electron ionization energy and electron affinities, respectively. Herein, we mainly used AIP and AEA, as shown in Table 1, to calculate $\eta$ of these designed 2D isomers, which is shown in Table 3.

The results indicated that the $\eta$ values of these 2D isomers are almost the same as **Y6**, which indicated that the chemical stability of 2D NFAs is similar to that of 1D linear NFAs. The $\eta$ value of **d-2D-ICH** (1.75) is the largest one in these isomers, indicating that **d-2D-ICH** has the highest chemical stability, even larger than that of **Y6**.

## Conclusions

In conclusion, we have investigated the isomerization stratagem of 2D NFAs by isomerizing the conjugated backbone. Three 2D isomers, namely, **2D-ICH**, **d-2D-ICH**, and **b-2D-ICH**, were constructed by an isomerized 2D fused-ring core and four difluorinated 1,1-dicyanomethylene-3-indanone. Compared with the famous acceptor material **Y6**, these 2D isomers exhibit a lower LUMO energy level and a stronger electron affinity, which is conducive to the acceptance of electron. These 2D isomers exhibited broadened electron absorption spectrum and the integrated absorption intensity are larger than that of **Y6** with an order of **d-2D-ICH** > **b-2D-ICH** > **2D-ICH** > **Y6**. This indicates that these 2D isomers can effectively increase the absorption of solar radiation to generate more excitons. Simultaneously, they have smaller $E_c$ and $E_b$, which can facilitate the separation of excitons to produce more free charges. In addition, these 2D isomers show good electron mobility in the same order of magnitude as **Y6** and **d-2D-ICH** even exhibits higher mobility than that of **Y6**. This demonstrates that **d-2D-ICH** can transport the free electron more efficiently. Finally, these 2D isomers show good solubility in chlorobenzene, benzene, DMF and DMSO, which are sufficient to fabricate solution-processed OSCs. All these results indicate that in addition to the isomerization of side chains, the isomerism of conjugated backbone is also an efficient method to turn the optoelectronic properties of NFA materials. Simultaneously, considering the electron affinity, sunlight absorption, exciton separation, electron transportation, solubility and chemical stability, **d-2D-ICH** is suitable as an important candidate for the development of next-generation NFAs for high-performance OSCs.

## Conflicts of interest

There are no conflicts to declare.

## Acknowledgements

This work was supported by the Science and Technology Research Program of the Chongqing Education Commission of China (KJQN202001431 and KJQN202101412) and the Scientific Research Grants of Yangtze Normal University (2017XJQN04). We acknowledge the Hongzhiwei Technology (Shanghai) Co., Ltd for providing the computational resources.

## References

1 L. Dou, Y. Liu, Z. Hong, G. Li and Y. Yang, *Chem. Rev.*, 2015, **115**, 12633–12665.
2 C. Yan, S. Barlow, Z. Wang, H. Yan, A. K. Y. Jen, S. R. Marder and X. Zhan, *Nat. Rev. Mater.*, 2018, **3**, 18003.
3 H. Fu, Z. Wang and Y. Sun, *Angew. Chem., Int. Ed.*, 2019, **58**, 4442–4453.
4 B. Qiu, Z. Chen, S. Qin, J. Yao, W. Huang, L. Meng, H. Zhu, Y. Yang, Z.-G. Zhang and Y. Li, *Adv. Mater.*, 2020, **32**, 1908373.
5 G.-U. Kim, C. Sun, J. S. Park, H. G. Lee, D. Lee, J.-W. Lee, H. J. Kim, S. Cho, Y.-H. Kim, S.-K. Kwon and B. J. Kim, *Adv. Funct. Mater.*, 2021, **31**, 2100870.
6 J. Yuan, Y. Zhang, L. Zhou, G. Zhang, H.-L. Yip, T.-K. Lau, X. Lu, C. Zhu, H. Peng, P. A. Johnson, M. Leclerc, Y. Cao, J. Ulanski, Y. Li and Y. Zou, *Joule*, 2019, **3**, 1140–1151.
7 Y. Yang, Z.-G. Zhang, H. Bin, S. Chen, L. Gao, L. Xue, C. Yang and Y. Li, *J. Am. Chem. Soc.*, 2016, **138**, 15011–15018.
8 B. Fan, D. Zhang, M. Li, W. Zhong, Z. Zeng, L. Ying, F. Huang and Y. Cao, *Sci. China: Chem.*, 2019, **62**, 746–752.
9 Q. Liu, Y. Jiang, K. Jin, J. Qin, J. Xu, W. Li, J. Xiong, J. Liu, Z. Xiao, K. Sun, S. Yang, X. Zhang and L. Ding, *Sci. Bull.*, 2020, **65**, 272–275.
10 Y. Cheng, B. Huang, X. Huang, L. Zhang, S. Kim, Q. Xie, C. Liu, T. Heumüller, Z. Liu, Y. Zhang, F. Wu, C. Yang, C. J. Brabec, Y. Chen and L. Chen, *Angew. Chem., Int. Ed.*, 2022, e202200329.
11 G. Han, Y. Guo, L. Ning and Y. Yi, *Sol. RRL*, 2018, **0**, 1800251.

 

12 Y. Cui, Y. Xu, H. Yao, P. Bi, L. Hong, J. Zhang, Y. Zu, T. Zhang, J. Qin, J. Ren, Z. Chen, C. He, X. Hao, Z. Wei and J. Hou, *Adv. Mater.*, 2021, **33**, 2102420.
13 M. Liu, P. Fan, Q. Hu, T. P. Russell and Y. Liu, *Angew. Chem., Int. Ed.*, 2020, **59**, 18131–18135.
14 Y. Liu, C. e Zhang, D. Hao, Z. Zhang, L. Wu, M. Li, S. Feng, X. Xu, F. Liu, X. Chen and Z. Bo, *Chem. Mater.*, 2018, **30**, 4307–4312.
15 Z. Luo, R. Sun, C. Zhong, T. Liu, G. Zhang, Y. Zou, X. Jiao, J. Min and C. Yang, *Sci. China: Chem.*, 2020, **63**, 361–369.
16 Y. Wang, J. Lee, X. Hou, C. Labanti, J. Yan, E. Mazzolini, A. Parhar, J. Nelson, J.-S. Kim and Z. Li, *Adv. Energy Mater.*, 2021, **11**, 2003002.
17 A. Wadsworth, H. Bristow, Z. Hamid, M. Babics, N. Gasparini, C. W. Boyle, W. Zhang, Y. Dong, K. J. Thorley, M. Neophytou, R. S. Ashraf, J. R. Durrant, D. Baran and I. McCulloch, *Adv. Funct. Mater.*, 2018, **0**, 1808429.
18 Y. Lin, T. Li, F. Zhao, L. Han, Z. Wang, Y. Wu, Q. He, J. Wang, L. Huo, Y. Sun, C. Wang, W. Ma and X. Zhan, *Adv. Energy Mater.*, 2016, **6**, 1600854.
19 H. Bristow, K. J. Thorley, A. J. P. White, A. Wadsworth, M. Babics, Z. Hamid, W. Zhang, A. F. Paterson, J. Kosco, J. Panidi, T. D. Anthopoulos and I. McCulloch, *Adv. Electron. Mater.*, 2019, **5**, 1900344.
20 C. Yao, Y. Yang, L. Li, M. Bo, C. Peng and J. Wang, *J. Mater. Chem. A*, 2019, **7**, 18150–18157.
21 Y. Yang, C. Yao, L. Li, M. Bo, J. Zhang, C. Peng, Z. Huang and J. Wang, *Dyes Pigm.*, 2020, **181**, 108542.
22 R. J. Ouellette and J. D. Rawn, 2 - Functional Groups and Their Properties. in *Organic Chemistry*, ed., R. J. Ouellette, J. D. Rawn, Academic Press, 2nd edn, 2018, pp 31–49.
23 E. Caldeweyher, C. Bannwarth and S. Grimme, *J. Chem. Phys.*, 2017, **147**, 034112.
24 S. Grimme, S. Ehrlich and L. Goerigk, *J. Comput. Chem.*, 2011, **32**, 1456–1465.
25 D. Aravena, M. Atanasov and F. Neese, *Inorg. Chem.*, 2016, **55**, 4457–4469.
26 E. R. Johnson, S. Keinan, P. Mori-Sánchez, J. Contreras-García, A. J. Cohen and W. Yang, *J. Am. Chem. Soc.*, 2010, **132**, 6498–6506.
27 T. Lu and F. Chen, *J. Comput. Chem.*, 2012, **33**, 580–592.
28 F. Neese, *Wiley Interdiscip. Rev.: Comput. Mol. Sci.*, 2012, **2**, 73–78.
29 C. Yao, L. Xin, Y. Yang, L. Li, M. Bo, C. Peng and J. Wang, *J. Mater. Chem. A*, 2022, DOI: **10.1039/D2TA03728A**.
30 P. E. Blöchl, *Phys. Rev. B: Condens. Matter Mater. Phys.*, 1994, **50**, 17953–17979.
31 D. Studio, *Device Studio, 2021A*, Hongzhiwei Technology, China, 2021.
32 J. Wang, R. M. Wolf, J. W. Caldwell, P. A. Kollman and D. A. Case, *J. Comput. Chem.*, 2004, **25**, 1157–1174.
33 R. A. Marcus, *Rev. Mod. Phys.*, 1993, **65**, 599–610.
34 J. Ridley and M. Zerner, *Theor. Chim. Acta*, 1973, **32**, 111–134.
35 C. Yao, C. Peng, Y. Yang, L. Li, M. Bo and J. Wang, *J. Mater. Chem. C*, 2018, **6**, 4912–4918.
36 C. Yao, C. Peng, Y. Yang, L. Li, M. Bo and J. Wang, *J. Phys. Chem. C*, 2018, **122**, 22273–22279.
37 C. Yao, Y. Yang, L. Li, M. Bo, C. Peng and J. Wang, *J. Mater. Chem. C*, 2018, **6**, 6146–6152.
38 C. Janiak, *J. Chem. Soc., Dalton Trans.*, 2000, 3885–3896.
39 W. Zhao, S. Li, H. Yao, S. Zhang, Y. Zhang, B. Yang and J. Hou, *J. Am. Chem. Soc.*, 2017, **139**, 7148–7151.
40 J.-C. Lee, J.-D. Chai and S.-T. Lin, *RSC Adv.*, 2015, **5**, 101370–101376.
41 T.-J. Wen, Z.-X. Liu, Z. Chen, J. Zhou, Z. Shen, Y. Xiao, X. Lu, Z. Xie, H. Zhu, C.-Z. Li and H. Chen, *Angew. Chem., Int. Ed.*, 2021, **60**, 12964–12970.